Ray dynamics and wave chaos in circular-side polygonal microcavities

Min Tang, Yue-De Yang,* Hai-Zhong Weng, Jin-Long Xiao, and Yong-Zhen Huang†

State Key Laboratory of Integrated Optoelectronics, Institute of Semiconductors, Chinese Academy of Sciences, Beijing 100083, China and Center of Materials Science and Optoelectronics Engineering, University of Chinese Academy of Sciences, Beijing 100049, China

(Received 11 November 2018; published 6 March 2019)

We systematically study mode characteristics in circular-side polygonal microcavities (CSPMs), particularly in these cavities with chaotic ray dynamics, in order to gain insights into the wave chaos in the CSPMs. The circular sides could improve the light confinement of the CSPMs as concave mirrors, in that regular islands are formed around the stable fixed points in the Poincaré surface of sections (SOS). However, the fixed points become unstable under some specific deformations, and global chaos with quasistable "star islands" appears around these fixed points in the Poincaré SOS accordingly. The phenomenon can be well explained by the ray dynamic analysis under the second-order approximation, and the results show that the high-order terms play an important role in the motions of light rays and destroy the regular islands in the phase space leading to chaotic ray dynamics. The destruction of regular islands results in degradation of mode quality factors and dispersed mode field distributions according to the finite-element method simulation of the confined modes. Furthermore, an unusual variation of mode quality factor is observed by varying the refractive index of the outside media for the CSPM with chaotic ray dynamics.

DOI: 10.1103/PhysRevA.99.033814

I. INTRODUCTION

Whispering-gallery mode (WGM) optical microcavities, which confine light rays by continuous total internal reflections (TIRs) at the cavity boundaries, have attracted great attention in both fundamental physics studies and practical device applications [1–4]. By storing optical energy in small volumes, the WGM microcavities could greatly enhance the light-matter interactions [5–7] and the phonon-photon coupling [8–10]. Among the WGM microcavities with various shapes, circular microcavities with a circularly symmetric geometry have achieved the most successes in the demonstration of ultralow-threshold microlasers, thanks to their ultrahigh-quality (Q) WGMs [11,12]. However, the circular rotational symmetry results in homogeneous lasing emission along the cavity rim, which limits the practical applications of the circular microcavity lasers in photonic integration. Especially for the semiconductor microcavities, the Q factors of the WGMs are typically limited by both the material absorption and the vertical radiation losses [13]. Thus designing a cavity shape to properly break the rotational symmetry is required to achieve efficient in-plane directional emission with moderately high Q factor [14].

Various asymmetric resonant cavities (ARCs), including spiral-shaped cavity [15], limaçon cavity [16], and the "Face" cavity [17], have been proposed and demonstrated experimentally for realizing directional emission. The mechanism of directional emission for the ARCs is explained as chaos-assisted tunneling (CAT) and unstable manifolds escape, which is the heart of quantum chaos and nonlinear dynamics in an open system [18–22]. Chao-assisted channeling (CAC) was proposed and proved to realize directional emission from the chaotic microcavities with long-lived resonances [23]. Besides realizing directional emission, the chaotic ARCs were also demonstrated to achieve broadband and fast momentum transformation [24], enhance energy storage [25], and suppress spatiotemporal instabilities [26]. In addition, the wave chaos in ARCs affected the competition between the lasing modes and resulted in single-mode operation [27,28].

Apart from the ARCs with smooth boundaries, WGM microcavities with regular polygonal shapes have also been investigated intensively due to their special mode properties [29–37]. Recently, we proposed and demonstrated circular-side square microcavity semiconductor lasers to enhance the mode Q factors and the transverse mode interval simultaneously, and suppress the undesired high-order transverse modes [38,39]. The circular sides introduce an additional degree of freedom for manipulating the WGMs in circular-side polygonal microcavities (CSPMs), and may lead to novel applications of these microcavities. However, there is still a lack of a global understanding for the regulation mechanism of the WGMs in the CSPMs. In this paper, we systematically study the ray dynamics and the corresponding wave solutions for the CSPMs, particularly the cavities with chaotic ray dynamics. The orbits connecting the midpoints of the sides are inherent periodic orbits (POs) of the CSPMs, which appear as fixed points in the Poincaré surface of sections (SOSs). Based on the analyses of the ray dynamics, the circular sides of the CSPMs typically lead to regular islands around the stable fixed points in the Poincaré SOSs. The size of the islands varies with the deformation parameter. Interestingly, a transition of POs from stable to unstable is observed under a few specific deformations, and global chaos appears as the regular islands degrade to quasistable "star islands." The

*yyd@semi.ac.cn
†yzhuang@semi.ac.cn

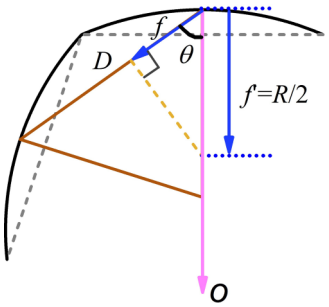

FIG. 1. Schematic diagram of two adjacent sides of a CSPM.

unstable POs, which form scarred modes in microcavities [40–42], were first investigated in the subject of chaos [43,44] and later extended to photonics research [16,18]. Unstable POs could also arise from the local perturbations of an integrated billiard, and lied in the chaotic sea as marginally unstable POs [45,46]. Compared with the unstable POs reported before, the star islands result from high-order terms in paraxial approximation, and therefore are relatively stable occupying a large area in the phase space, which is a benefit for the formation of long-lived modes. The destruction of the boundary between the islands and the chaotic sea allows direct transfer between the photons in these two regions, which may dramatically affect the confined modes. The finite-element method (FEM) is performed to simulate the characteristics of the WGMs. Decreased mode Q factors and dispersed mode field distributions are observed for the WGMs in the CSPMs with chaotic ray dynamics, which can be well explained by the ray dynamic analyses.

II. RAY DYNAMIC ANALYSIS FOR THE CSPMs

A schematic diagram of two adjacent sides of a CSPM is shown in Fig. 1. For the sake of simplification, the other sides are not presented in the figure owing to the rotational symmetry of the CSPM. The cavity geometry is determined by the following three parameters: the side number of the regular polygonal microcavity N, the distance between the midpoints of adjacent sides D, and the deformation degree m defined as

$$m = D/f, \tag{1}$$

where f is the focal length along the line connecting the midpoints of adjacent sides as shown in Fig. 1. The focal length f can be obtained as $f = f'\cos(\theta) = R\cos(\theta)/2$, where f' and R are the paraxial focal length and the radius of circular sides, respectively, and θ is the incident angle of the light ray propagating along the line connecting the midpoints of adjacent sides. The CSPM is a regular polygonal microcavity with $m = 0$ and is a circular microcavity with $m = 4$. In the following discussion, we restrict the deformation degree m in the range from 0 to 4 covering all the shapes deformed from the regular polygonal microcavity to the circular microcavity.

Basically, varying the deformation degree m will not change the symmetry properties of the CSPMs. The confined modes can still be classified into irreducible representations of the point group C_{Nv}, which gives the general rules of the degeneracy of the WGMs [33]. Thus part of the double-degenerate modes will split into two nondegenerate standing-wave modes with different mode frequencies and Q factors. However, the converging effect of the circular-side concave mirrors will reduce the light scattering at the vertices greatly [38], and lead to a decrease of the differences in the mode frequencies and Q factors compared with the regular polygonal microcavities.

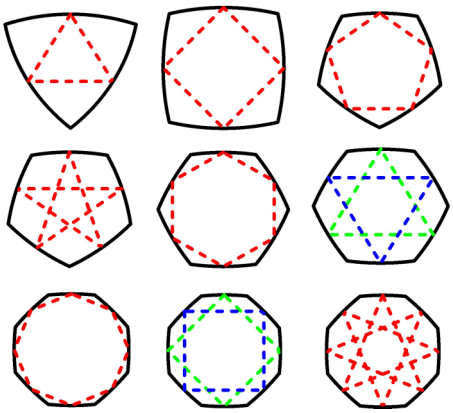

FIG. 2. POs of the CSPMs with $N = 3$, 4, 5, 6, and 8. The orbits marked by the blue and green dashed lines are degenerate orbits, and the orbits reflected between the opposite sides for the CSPMs with even side numbers are neglected.

We first study the influence of the side number N on the ray dynamics. The POs of the CSPMs with different side numbers of 3, 4, 5, 6, and 8 are shown in Fig. 2, where the orbits reflected between the opposite sides for the CSPMs with even N are neglected because these light rays cannot be totally reflected. Different from the regular polygonal microcavities, which have multiple periodic orbit families, the inevitable fixed orbits in the CSPMs are the light rays connected to the midpoints of the circular sides. Here we define l as the side-number difference between the ray-connected sides, and in the case $l = 1$ the light ray propagates between the adjacent sides, and the corresponding modes are denoted as adjacent reflection modes (ARMs). If the light ray returns to the initial side after p times of reflections, $lp = MN$ should be satisfied, where M is a positive integer. Then p can be solved as

$$p = \frac{N}{(N, l)}, \tag{2}$$

where (N, l) is the maximum common divisor of N and l. (N, l) is also the degeneracy of this type of POs, and it has proved useful in the formation of long-lived resonances [47–49]. For example, the orbits constructed by reflections between next-nearest-neighbor sides in the hexagonal microcavity are doubly degenerate, as shown in Fig. 2, which is coincident with (6, 2). We can derive that the number of periodic orbits for a CSPM is $\sum_{i=1}^{[N/2]}(N, i)$, where the square brackets is the rounding operation. The number of POs increases as N increases. If N is a prime number, the POs number is $(N - 1)/2$.

The analyses above reveal the regularity of POs in the CSPMs. In order to demonstrate the ray dynamics, the Poincaré SOSs of the CSPMs with $m = 1.5$, and $N = 3$, 4, 11, and 12 are calculated and shown in Figs. 3(a)–3(d),

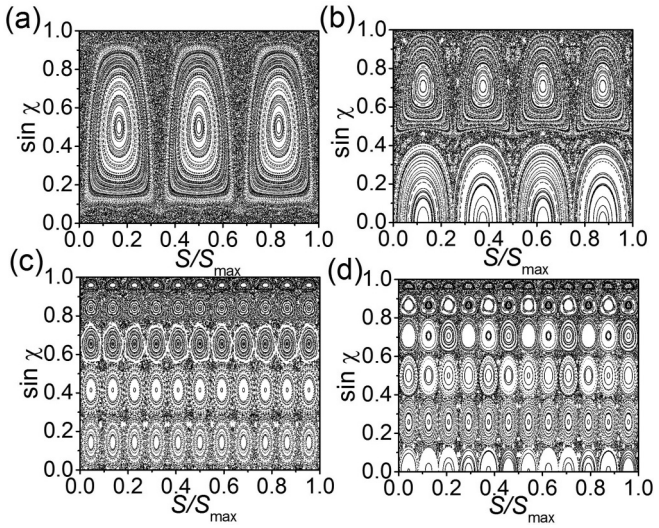

FIG. 3. Poincaré SOSs of the CSPMs with N = (a) 3, (b) 4, (c) 11, and (d) 12. The deformation degrees of the CSPMs are 1.5.

respectively, where χ is the incident angle of the light ray on the boundary, S is the distance from one of the vertices along the boundary in a counterclockwise direction, and $S_{\max}$ is the perimeter of the CSPM. In the calculation of the Poincaré SOS, we use 200 light rays with random initial conditions in the phase space and record the first 500 reflections for each ray. Only the upper half of the SOSs are shown in the figures, as the lower half will have similar structure due to the symmetry of the CSPMs.

In general, the phase space of a regular polygonal microcavity is constructed by segmented horizontal lines, and that of a circular microresonator is constructed by horizontal lines. The Poincaré SOSs of a square microcavity and a circular cavity are illustrated in Figs. 4(a) and 4(b), respectively. In the SOSs of the CSPMs, these orbits evolve into many regular islands arranged in an array, and chaotic sea appears around the islands. From the top to the bottom of the phase space, each row of the islands represents the POs with l varied from 1 to $[N/2]$. Figures 3(a) and 3(c) show the SOSs of the CSPMs with N equaling prime numbers of 3 and 11, where 1 and 5 kinds of nondegenerate orbits are observed and the islands on the same horizontal line have similar structure. For the case $N = 4$ as shown in Fig. 3(b), there is a nondegenerate orbit reflected by the adjacent sides (top islands with $l = 1$) and double-degenerate orbits reflected by the opposite sides (bottom islands with $l = 2$). For the case $N = 12$ as shown in Fig. 3(d), the islands on the same horizontal line have a variety of structures and the degeneracies from the top islands to the bottom islands are 1, 2, 3, 4, 1, and 6, respectively.

When the side number is fixed, the cavity shape can be changed by varying the deformation degree m, and the ray dynamics will be modulated accordingly. In the following discussion, we mainly consider the ARMs with the light ray reflections between the adjacent sides of the CSPMs, as these light rays have the largest incident angle benefiting the TIR. A 2×2 monodromy matrix $T(m)$ for the reflections between the adjacent sides around the midpoints under the first-order paraxial approximation is obtained as (the axis is chosen as

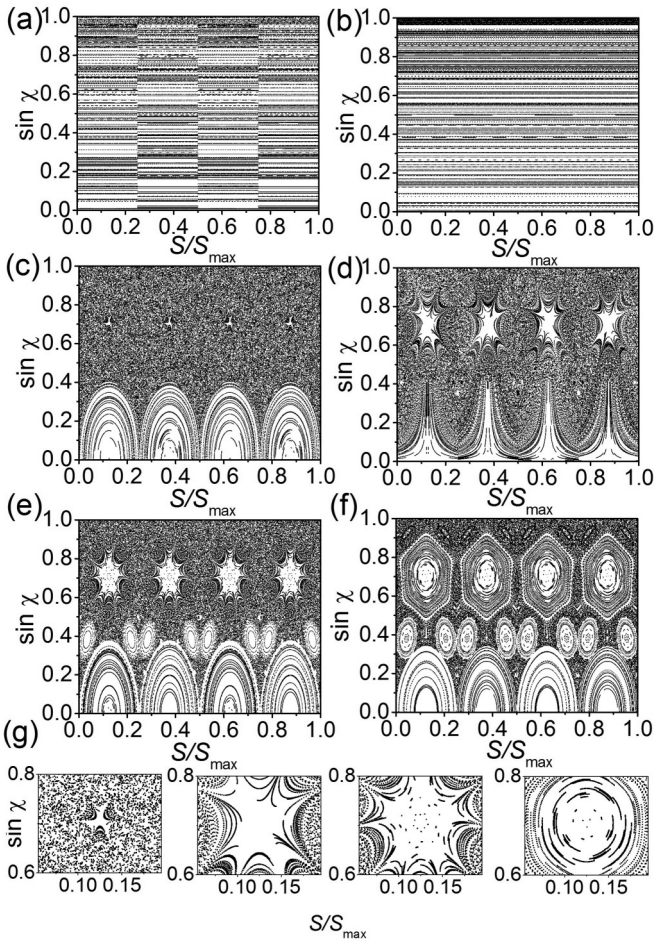

FIG. 4. Poincaré SOSs of (a) a square microcavity, (b) a circular cavity, and the CSPMs with $N = 4$ and m = (c) 1, (d) 2, (e) $(3+\sqrt{5})/2$, and (f) 3. (g) Zoom-in view of the regions around the island center of the SOSs shown in (c)–(f).

the line connecting the midpoints of the adjacent sides)

$$\begin{pmatrix} \frac{\delta\phi_{j+1}}{D} \\ \frac{\delta\theta_{j+1}}{\sin(\pi/N)} \end{pmatrix} = \begin{pmatrix} \frac{m}{2}-1 & -\sqrt{2} \\ \frac{m}{\sqrt{2}}-\frac{m^2}{4\sqrt{2}} & \frac{m}{2}-1 \end{pmatrix} \begin{pmatrix} \frac{\delta\phi_j}{D} \\ \frac{\delta\theta_j}{\sin(\pi/N)} \end{pmatrix}, \quad (3)$$

where $\delta\phi_j$ and $\delta\theta_j$ are the position offset and the incident angle offset, respectively. The determinant of $T(m)$ equals 1. Similar to the steady condition in the coaxial spherical cavity, $T(m)$ should satisfy the same stability condition that the half of the sum of the matrix diagonals is between -1 and 1 [50]. Thus, the stable condition can be obtained as $0 < m < 4$, which means that the CSPM considered here is always a stable cavity for the paraxial light rays under the first-order approximation. The mapping relation in Eq. (3) results in concentric ellipses in the SOS except for some specific deformations that we will discuss below.

One interesting phenomenon is the generation of fixed points under the evolution of the ray trajectories. The condition $[T(m)]^r = I$ can give a sequence m_r with $r \geqslant 3$, where I is the identity matrix. The corresponding m_r can be obtained as [50]

$$m_r = 2\cos(2q\pi/r) + 2, \quad (4)$$

where q is a positive integer satisfying $q < r/2$. Then the incident angle offsets and the position offsets will loop after r times of reflections. Each regular island will degenerate to discrete fixed points with a number of $r/(r, N)$ for a single ray trajectory, where (r, N) is the maximum common divisor of r and N. The Poincaré SOSs of the CSPMs with $N = 4$ and $m = 1,\ 2,\ (3 + \sqrt{5})/2$, and 3 corresponding to m_3, m_4, m_5, and m_6 are presented in Figs. 4(c)–4(f), respectively. Based on the transmission analysis under the first-order approximation, the fixed points will appear as triple, single, quintuple, and triple patterns near the center of each island, which is verified by the zoom-in view of the island center as shown in Fig. 4(g) considering the rotational symmetry. However, the island centers of the SOSs are not exactly discrete fixed points. With the deformation degrees of m_3, m_4, and m_5, the islands degenerate to hyperbolalike curves, and the light rays become unstable even for these rays close to the island center. In a SOS, the regions are always separated as Kolmogorov-Arnold-Moser (KAM) curves, chaotic seas, and closed islands. The islands in Figs. 4(c)–4(e) are different from these three situations, and we term the quasistable islands with discrete fixed points as the star islands. As these islands are no longer stable, a transition to global chaos is observed for the four-bounced light rays in the CSPMs with these specific deformations. In addition, hexagonal-shaped regular islands could be identified in Fig. 4(f) with the deformation degree of m_6. The star islands in the CSPMs are similar to the unstable POs along the long axes of ellipses [51], but are much more stable. The reason is that Eq. (3) under first-order paraxial approximation gives stable and unstable motions for the POs in CSPMs and ellipses, respectively, which indicate that the unstable motion of the star islands may result from high-order terms.

According to the above discussion, the Poincaré SOSs show unstable ray dynamics under some specific deformations, which are conflicted with the analytical results under the first-order paraxial approximation. The motion of the ray trajectories in the phase space should be guided by the high order of mapping relations for the fixed points. The mapping from $(\delta\phi_j, \delta\theta_j)$ to $(\delta\phi_{j+1}, \delta\theta_{j+1})$ considering the second-order terms can be expressed as

$$\begin{aligned}\delta\theta_j = \sin\left(\frac{\pi}{N}\right)\Bigg[&\left(\frac{m}{2}-1\right)\frac{\delta\phi_j}{D} - \frac{\delta\phi_{j+1}}{D} + \left(\frac{m}{4}-1\right)\\ &\times\cos\left(\frac{\pi}{N}\right)\frac{\delta\phi_j^2}{D^2} - \left(\frac{m}{4}-1\right)\cos\left(\frac{\pi}{N}\right)\frac{\delta\phi_{j+1}^2}{D^2}\Bigg],\\ \delta\theta_{j+1} = \sin\left(\frac{\pi}{N}\right)\Bigg[&\frac{\delta\phi_j}{D} - \left(\frac{m}{2}-1\right)\frac{\delta\phi_{j+1}}{D} - \left(\frac{m}{4}-1\right)\\ &\times\cos\left(\frac{\pi}{N}\right)\frac{\delta\phi_j^2}{D^2} + \left(\frac{m}{4}-1\right)\cos\left(\frac{\pi}{N}\right)\frac{\delta\phi_{j+1}^2}{D^2}\Bigg].\end{aligned} \tag{5}$$

The detailed derivation process could be found in the Appendix. We restrict the initial conditions near the center of the island and calculate the SOS in the phase space for the CSPM with $N = 4$ and $m = 1$. We calculated 500 ray trajectories with random initial condition confined in a square region with a normalized side length of 5×10^{-3} and centered at one of the fixed points in the SOS. Each ray trajectory is reflected for 500 times. The SOSs obtained without approximation and with second-order approximation are calculated and shown in Figs. 5(a) and 5(b), respectively. We could identify mutually similar fractal structures in Figs. 5(a) and 5(b), which is the center of the star islands. The results show that Eq. (5) under the second-order approximations can give good characterization of the ray trajectories. The schematic diagram of the motion of the ray trajectories around the star islands is plotted in Fig. 5(c), which could be verified by calculating the single ray in Fig. 5(a) or 5(b). The star island is not a conservative system and ray trajectories will move out of the islands in the directions as the arrows present. Besides, the ray trajectories will move in the islands in other directions. Different from the regular islands in a SOS, the star islands have leakage channels directly coupled to the chaotic sea through the high-order terms of the transformation matrix.

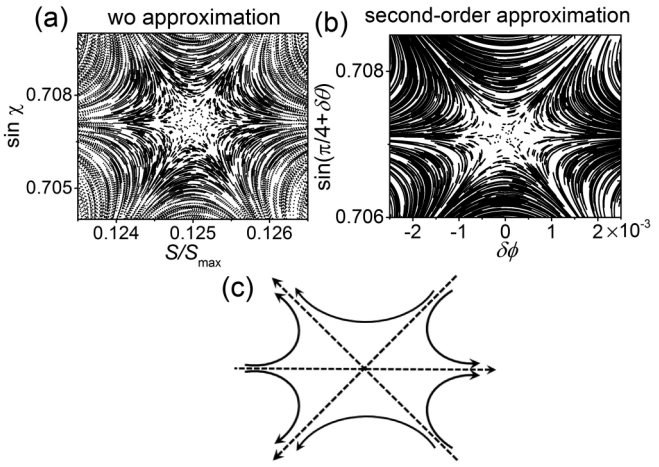

FIG. 5. Fractal structures of the star islands in CSPM with $N = 4$ and $m = 1$. (a) Star islands calculated by strict SOS, (b) star islands calculated under second-order approximation, and (c) schematic diagram of the motions of the ray trajectories for the star islands.

Furthermore, the second-order approximation still gives discrete fixed points for the star islands with $m = m_4$ and m_5, which means that the unstable motion of the light rays may arise from the higher-order terms. The relatively large white areas of these star islands, as shown in Fig. 4(g), also indicate high stability for the light rays around the island center. Although the ray dynamics in the star islands is not stable as with the regular islands, the lifetimes of the corresponding light rays are much longer than that of the light rays in the chaotic sea, which indicates that moderately high Q modes may exist in the CSPMs with chaotic ray dynamics. Furthermore, similar ray dynamics relative to the deformation degree are observed for the CSPMs with different side numbers.

III. NUMERICAL SIMULATIONS OF CSPMs

For the two-dimensional (2D) WGM microcavities with a refractive index distribution of $n(x, y)$, the Maxwell's equations for the confined optical field can be replaced by the

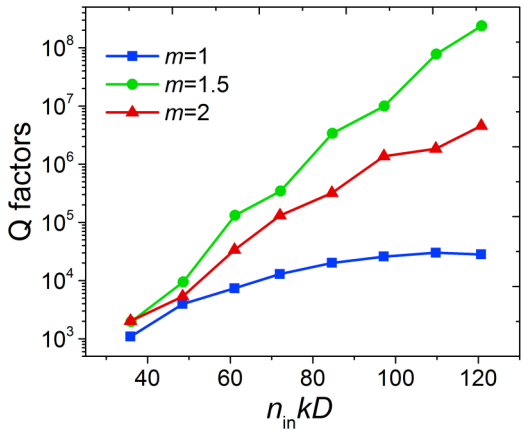

FIG. 6. Mode Q factors vs normalized size of the CSPMs with $N = 4$ and $m = 1$, 1.5, and 2.

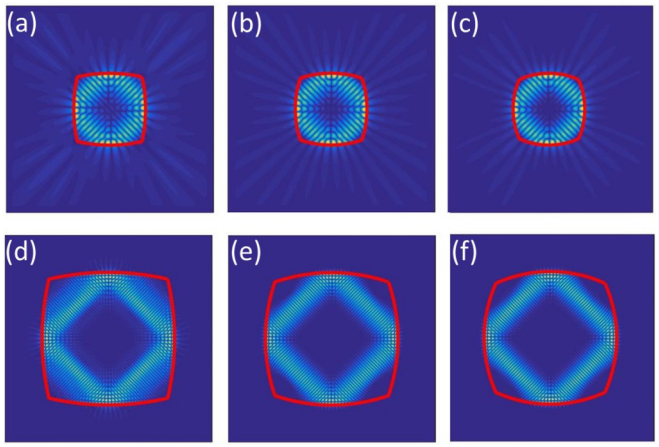

FIG. 7. |Hz| field distributions of the modes in the CSPMs with $D = 3\,\mu$m and (a) $m = 1$, (b) $m = 1.5$, (c) $m = 2$, and $D = 10\,\mu$m and (d) $m = 1$, (e) $m = 1.5$, and (f) $m = 2$. The red lines show the boundary of the CSPMs.

scalar wave equation

$$-\nabla^2\psi(x,y) = n^2(x,y)\frac{\omega^2}{c^2}\psi(x,y), \tag{6}$$

where ω is the angular frequency, c is the light speed in vacuum, and ψ represents the field distribution. We numerically simulate the transverse-electric (TE) polarized modes in the CSPMs by the FEM (COMSOL MULTIPHYSICS 5.0) to verify the above analyses of the ray dynamics and explore their impact on the mode characteristics. A perfectly matched layer with a width of 0.5 μm is used to absorb the outgoing waves and terminate the simulation window. The maximum grid sizes are set as $\lambda/6n$ to ensure the computation accuracy, where λ is the mode wavelength and n is the refractive index. The refractive indices of the CSPMs (n_{in}) and outside media (n_{out}) are set to 3 and 1.5, respectively. The mode Q factors can be extracted from the obtained complex mode frequency through $Q = \mathrm{Re}(\omega)/|2\mathrm{Im}(\omega)|$.

The Q factors of the fundamental transverse modes in the CSPMs with $N = 4$ and different m are plotted as functions of normalized cavity size ($n_{in}kD$). In the simulation, D is varied from 3 to 10 μm, and the wavelengths of the selected modes are kept around 1550 nm. With $m = 1$, the CSPMs is close to a chaotic cavity, as shown in Fig. 4(c), and the Q factor increases from 1.1×10^3 to 2.8×10^4 as the cavity size increases from 3 to 10 μm. The slope of the curve shows a saturation of the Q factors and also exhibits a decrease trend with the further increase of the cavity size, as mode light can escape from the star islands quickly. For the CSPMs with $m = 1.5$, the modes are confined in the regular island, as shown in Fig. 3(b), and the Q factor increases dramatically from 2.0×10^3 to 2.4×10^8 with the increase of cavity size. For the CSPMs with $m = 2$ and the ray dynamics as shown in Fig. 4(d), the Q factor increases from 2.0×10^3 to 4.6×10^6. In such situation, the ray dynamics of CSPMs is also chaotic, but the instability of ray dynamics induced by higher-order terms of the transmission matrix and the areas of the islands are larger than CSPMs with $m = 1$, as shown in Fig. 4(g). Thus the light confinement and Q factors are between the two situations above.

Figure 7 shows the magnetic field ($|H_z|$) distributions of the fundamental transverse WGMs in the CSPMs with $N = 4$. The magnetic fields of simulated modes are antisymmetric and symmetric relative to the x and y axes, respectively. Figures 7(a)–7(c) show the field distributions of the modes in the CSPMs with $D = 3\,\mu$m and $m = 1$, 1.5, and 2, respectively. The field distributions and scattering fields around the microcavities show similar structures. When D increases to 10 μm, the scattering fields are much weaker. Figures 7(d)–7(f) show the field distributions of the modes in the CSPMs with $D = 10\,\mu$m and $m = 1$, 1.5, and 2, respectively. A dispersed mode field distribution is found in Fig. 7(d), which indicates the wave chaos and high mode loss. As a comparison, the field distributions shown in Figs. 7(e) and 7(f) for the CSPMs with $m = 1.5$ and 2 indicate better mode confinement. The mode field distributions are consistent with the Q factor variation shown in Fig. 6.

Figure 8 shows the mode Q factors and the wavelengths of the ARMs in the CSPMs versus the deformation degree m. In the simulation, ND is kept as a constant. The Q factors exhibit a dip around $m = 1$ due to the chaotic ray dynamics for the CSPMs with different N. In the case of $ND = 50\,\mu$m, the lowest Q factors are 1.2×10^4, 4.7×10^3, 3.1×10^3, 2.0×10^3 at the deformation degrees of 1.1, 1, 1, and 0.9, and the highest Q factors are 1.4×10^{10}, 1.1×10^8, 3.2×10^5, and 1.0×10^4 for the CSPMs with $N = 4, 5, 6$, and 7, respectively. The CSPM with $N = 8$ show a positive correlation relation between the Q factor and m. In the case of $ND = 100\,\mu$m, the lowest Q factors are 1.1×10^4, 1.0×10^4, 4.5×10^3, 3.3×10^3, and 4.3×10^3 at the deformation degrees of 1, 1, 1.1, 1.1, and 1.2, and the highest Q factors are 2.9×10^{10}, 7.2×10^{10}, 3.0×10^8, 8.3×10^5, and 1.1×10^4 for the CSPMs with $N = 4$, 5, 6, 7, and 8, respectively. The ray dynamics analyses predict the degradation of the mode Q factors around $m = 1$, which agrees well with FEM simulation results with a slight difference in position where the lowest Q appears. When the side number N increases, the optical path will be closer to the vertices, resulting in the increase of pseudointegrable leakage and the decrease of Q factors [31]. Thus the ARMs

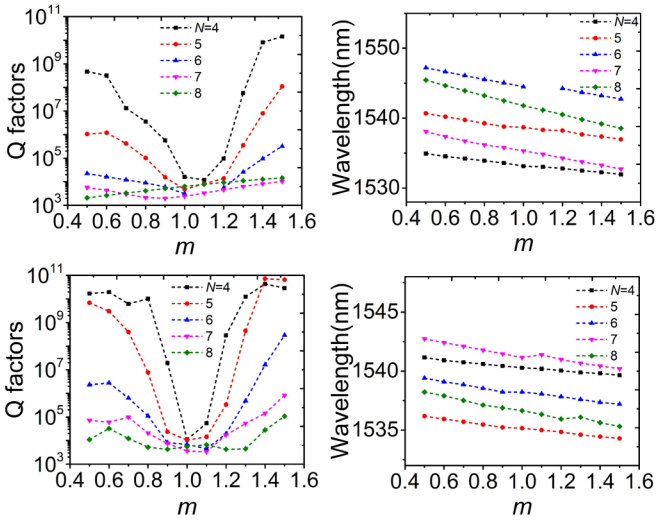

FIG. 8. (a) Mode Q factors and (b) mode wavelengths of the ARMs vs the deformation degree m in the CSPMs with $ND = 50\,\mu$m, and $N = 4, 5, 6, 7$, and 8. (c) Mode Q factors and (d) mode wavelengths of the ARMs vs the deformation degree m in the CSPMs with at $ND = 100\,\mu$m, and $N = 4, 5, 6, 7$, and 8. For the CSPM with $N = 8$ and $m = 1.1$, the ARMs are coupled with other modes and we cannot derive the Q factors and wavelengths directly.

are not necessarily the mode groups with the highest Q factors in the CSPMs with $N > 4$ [49]. Figures 8(b) and 8(d) shows a negative correlation between the mode wavelengths of ARMs and m. The reason is that the effective cavity area decreases with the increase of m when N and D are kept as a constant. A change of the slope is found around $m = 1$ due to the large variation of field distributions caused by the chaotic ray dynamics.

To further support our claim of the motions for the star islands in the phase space, we project two typical modes onto the phase space using the Husimi function [52,53]. The Husimi projections of the chaotic mode and the four-island mode are shown in Figs. 9(a) and 9(b), respectively, and the corresponding mode patterns are shown in the insets. Here the refractive index of outside media is decreased to 1 to better

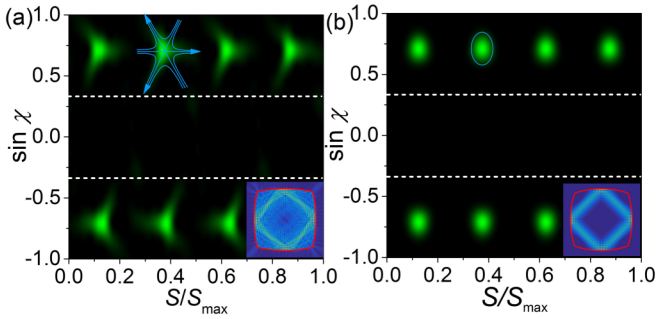

FIG. 9. Husimi projections of the ARMs in the CSPMs with m = (a) 1 and (b) 1.5. Insets show the corresponding |Hz| field distributions. The (a) blue arrows and (b) circle embedded in the second top island are diagrams of the flow of the ray trajectories in the phase space.

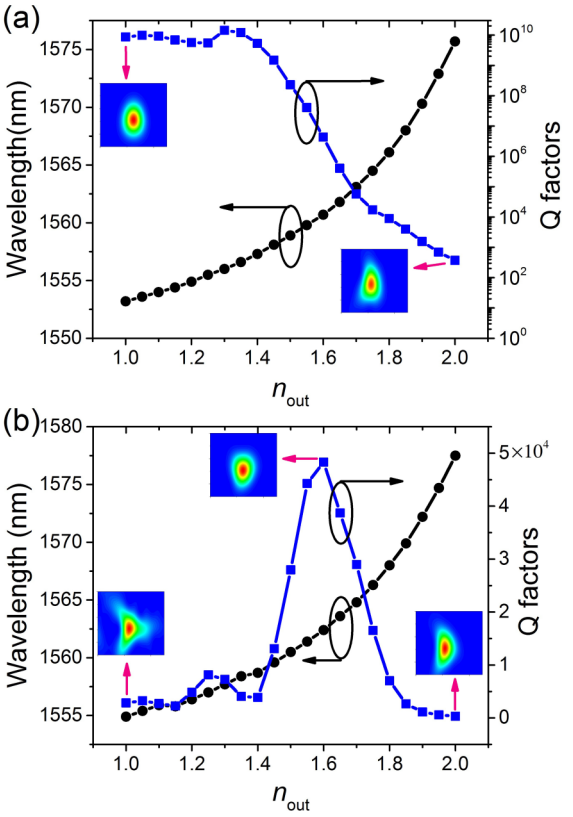

FIG. 10. Mode Q factors and mode wavelengths of the ARMs in the CSPMs with $N = 4$, $D = 10\,\mu$m, and $m =$ (a) 1.5 and (b) 1 vs the refractive index of outside media. The insets give the island shapes for the Husimi projections.

exhibit the chaotic mode. The geometries of the cavities are the same as that shown in Figs. 7(d) and 7(e), and the increase of the degree of chaos is revealed due to the increased refractive index contrast. The corresponding Q factors are 2.9×10^3 and 4.4×10^{10}, respectively. In both situations, the islands are centered at $\chi = \pm 45^\circ$ and $S/S_{max} = 1/8,\ 3/8,\ 5/8$, and $7/8$. The islands in the top of Fig. 9(a) are right-hand triangles and in the bottom are left-hand triangles; the angle-oriented positions for the star islands are the same with outgoing directions of the star island presented in Fig. 5(c). As a comparison, the islands in Fig. 9(b) are well isolated from the chaotic sea resulting in extremely high Q factor.

We consider the microcavities with different refractive index contrast to further identify the modes in the CSPMs with chaotic ray dynamics, which may give another perspective of the mode characteristics. Figures 10(a) and 10(b) show the mode Q factors and wavelengths of the ARMs in the CSPMs with $N = 4$, $D = 10\,\mu$m, and $m = 1.5$ and 1, respectively. The insets show the island shapes of the Husimi projections for the corresponding modes. The mode wavelengths increase when the refractive index of outside media is increased, due to the weakened mode confinement. However, the variation of Q factor is not a simple monotonic relation. For the mode with regular island ray dynamics shown in Fig. 10(a), the Q factor is essentially unchanged with the order of 10^{10} as n_{out} is increased from 1 to 1.4, which may be limited by the accuracy of the numerical simulation. When the refractive

index is increased further, the Q factor decreases dramatically as the islands are exposed beneath the TIR condition. For the mode with chaotic ray dynamics shown in Fig. 10(b), a peak around $n_{\text{out}} = 1.6$ appears in the variation of Q factors. The reason for the decrease of Q factors for large n_{out} is the same as the nonchaotic cavity. The dominant loss is the incomplete reflection of the light rays close to the island center. Interestingly, if n_{out} decreases from 1.6 to 1, the Q factor decrease because of the strong coupling between the island centers and leakage channels, and the modes turns from regular orbit mode to chaotic mode. The dominant loss is the leakage loss through the channels, as shown in Fig. 5(c). The insets of Fig. 10(b) show the transform of the islands from ellipse to right oriented triangles, which is a sign of chaos and can be verified in Figs. 5(a) and 5(c). The oscillation of Q factors is induced by the mode coupling between different transverse modes, which also leads to the discontinuities in the variation of the mode wavelength.

IV. DISCUSSIONS AND CONCLUSIONS

In summary, we have studied the ray dynamics and wave chaos in the CSPMs. Unstable fixed points appear in the Poincaré SOSs of the CSPMs with specific deformations. The light rays around the island center can directly couple to chaotic sea in the phase space through the high-order terms in the transmission matrix. Such phenomena are found in the CSPMs with different side numbers and different deformation degrees. The unstable fixed points and surrounding ray trajectories form quasistable star islands with discrete fixed points around the island center based on the ray dynamics analyses. Although the light rays in the star island are not really stable, the lifetimes are relatively long, which can support moderately high Q modes in the CSPMs. The chaotic ray dynamics leads to triangle-shaped islands in the Husimi projection and dispersed mode field distributions according to the FEM simulation. The leakage through the outgoing channels is also influenced by the refractive index contrast of the microcavities, which may modulate the Q factors accordingly. The mechanism of the ray dynamics with star islands presented here is not restricted in the geometry of CSPMs, but can also be exploited to other microcavities with the local boundaries that fulfill the same reflection relationships.

ACKNOWLEDGMENTS

This work was supported by the Key Research Program of Frontier Sciences, Chinese Academy of Sciences (Grant No. QYZDJ-SSW-JSC002) and the National Natural Science Foundation of China (NSFC) (Grants No. 61527823 and No. 61875188).

APPENDIX: THE MAPPING RELATIONS FOR ADJACENT REFLECTION MODES

The fixed points usually support POs in the SOSs. Equations (3) and (5) describe the regularity of the ray trajectories surrounding the fixed points, which are derived from the mapping relations of the adjacent reflection modes (ARMs).

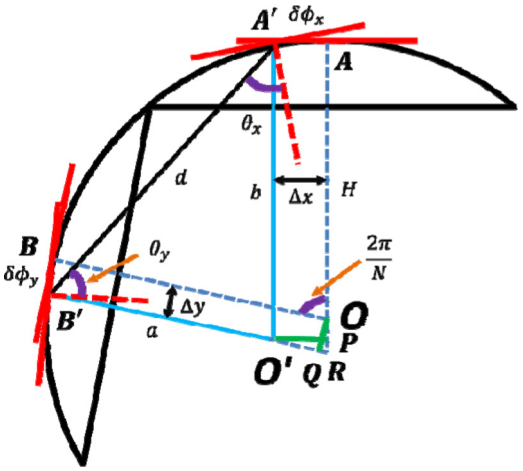

FIG. 11. Schematic diagram of the adjacent sides and single reflection rays. O is the center point of the CSPM; A and B are the center point of each curve side. $A'O'$ parallels to the AO and $B'O'$ parallels to BO. The extension cords of AO and $B'O'$ intersect at R. $O'P$ is perpendicular to AO, and OQ is perpendicular to BO.

As shown in Fig. 11, $AO = BO = H$, $B'O' = a$, $A'O' = b$, $A'B' = d$, $O'P = \Delta x$, $OQ = \Delta y$, $\overset{\frown}{AA'} = \delta\phi_x$, $\overset{\frown}{BB'} = \delta\phi_y$, $AP = h_x$, $B'Q = h_y$, the radius of the curve side is r, the angle between AO and BO is $2\pi/N$, and the reflection angles are θ_x and θ_y, respectively.

The position offsets are

$$\begin{aligned} \delta\phi_x &= r \arcsin(\Delta x/r), \\ \delta\phi_y &= r \arcsin(\Delta y/r). \end{aligned} \tag{A1}$$

For the triangle $A'B'O'$, the side lengths are expressed as

$$\begin{aligned} a &= h_y - \Delta x/\sin(2\pi/n_0) + \Delta y/\tan(2\pi/N), \\ b &= h_x + \Delta y/\sin(2\pi/n_0) - \Delta x/\tan(2\pi/N), \\ d &= [a^2 + b^2 - 2ab\cos(2\pi/N)]^{1/2}, \end{aligned} \tag{A2}$$

where $h_x = \sqrt{r^2 - \Delta x^2} - r + H$, $h_y = \sqrt{r^2 - \Delta y^2} - r + H$.

The angular offsets are

$$\begin{aligned} \delta\theta_x &= \arcsin[a\sin(2\pi/N)/d] \\ &\quad - \pi/2 + \pi/N + \arcsin(\Delta x/r), \\ \delta\theta_y &= \arcsin[b\sin(2\pi/N)/d] \\ &\quad - \pi/2 + \pi/N - \arcsin(\Delta y/r). \end{aligned} \tag{A3}$$

The Taylor series of position offsets to second order about Δx and Δy are

$$\begin{aligned} \delta\phi_x &= \left(\delta\phi_x + \frac{\partial\delta\phi_x}{\partial\Delta x}\Delta x + \frac{1}{2!}\frac{\partial^2\delta\phi_x}{\partial\Delta x^2}\Delta x^2\right)\Big|_{\Delta x=0} = \Delta x, \\ \delta\phi_y &= \left(\delta\phi_y + \frac{\partial\delta\phi_y}{\partial\Delta y}\Delta y + \frac{1}{2!}\frac{\partial^2\delta\phi_y}{\partial\Delta y^2}\Delta y^2\right)\Big|_{\Delta y=0} = \Delta y. \end{aligned} \tag{A4}$$

For the angular offsets, the Taylor series are

$$\delta\theta_x = \left(\frac{1}{r} - \frac{1}{2H}\right)\Delta x - \frac{1}{2H}\Delta y + \frac{(H-r)\cot(\pi/N)}{4H^2 r}\Delta x^2 - \frac{(H-r)\cot(\pi/N)}{4H^2 r}\Delta y^2,$$

$$\delta\theta_y = \frac{1}{2H}\delta\phi_x - \left(\frac{1}{r} - \frac{1}{2H}\right)\delta\phi_y - \frac{(H-r)\cot(\pi/N)}{4H^2 r}\delta\phi_x^2 + \frac{(H-r)\cot(\pi/N)}{4H^2 r}\delta\phi_y^2. \quad \text{(A5)}$$

Substitute (A4) into (A5) and we have relations

$$D = 2H\sin(\pi/N),$$

$$f = \frac{r}{2}\sin(\pi/N), \quad \text{(A6)}$$

$$D/f = m.$$

Then Eq. (5) can be obtained. As for Eq. (3), the squared terms in (A5) are neglected.

[1] K. J. Vahala, Nature (London) **424**, 839 (2003).
[2] L. N. He, S. K. Ozdemir, and L. Yang, Laser Photon. Rev. **7**, 60 (2013).
[3] H. Cao and J. Wiersig, Rev. Mod. Phys. **87**, 61 (2015).
[4] X. F. Jiang, C. L. Zou, L. Wang, Q. H. Gong, and Y. F. Xiao, Laser Photon. Rev. **10**, 40 (2016).
[5] K. Srinivasan and O. Painter, Nature (London) **450**, 862 (2007).
[6] E. Peter, P. Senellart, D. Martrou, A. Lemaître, J. Hours, J. M. Gérard, and J. Bloch, Phys. Rev. Lett. **95**, 067401 (2005).
[7] D. Alton, N. Stern, T. Aoki, H. Lee, E. Ostby, K. J. Vahala, and H. Kimble, Nat. Phys. **7**, 159 (2011).
[8] A. Schliesser, P. Del'Haye, N. Nooshi, K. J. Vahala, and T. J. Kippenberg, Phys. Rev. Lett. **97**, 243905 (2006).
[9] T. J. Kippenberg and K. J. Vahala, Science **321**, 1172 (2008).
[10] T. J. Kippenberg, H. Rokhsari, T. Carmon, A. Scherer, and K. J. Vahala, Phys. Rev. Lett. **95**, 033901 (2005).
[11] V. Sandoghdar, F. Treussart, J. Hare, V. Lefevre-Seguin, J.-M. Raimond, and S. Haroche, Phys. Rev. A **54**, R1777 (1996).
[12] B. Min, T. J. Kippenberg, L. Yang, K. J. Vahala, J. Kalkman, and A. Polman, Phys. Rev. A **70**, 033803 (2004).
[13] Y. D. Yang, Y. Z. Huang, and Q. Chen, Phys. Rev. A **75**, 013817 (2007).
[14] Z. X. Xiao, Y. Z. Huang, Y. D. Yang, J. L. Xiao, and X. W. Ma, Opt. Lett. **42**, 1309 (2017).
[15] G. Chern, H. Tureci, A. D. Stone, R. Chang, M. Kneissl, and N. Johnson, Appl. Phys. Lett. **83**, 1710 (2003).
[16] J. Wiersig and M. Hentschel, Phys. Rev. Lett. **100**, 033901 (2008).
[17] C. L. Zou, F. W. Sun, C. H. Dong, F. J. Shu, X. W. Wu, J. M. Cui, Y. Yang, Z. F. Han, and G. C. Guo, IEEE J. Sel. Top. Quantum Electron. **19**, 9000406 (2013).
[18] S. Shinohara, T. Harayama, T. Fukushima, M. Hentschel, T. Sasaki, and E. E. Narimanov, Phys. Rev. Lett. **104**, 163902 (2010).
[19] M. W. Kim, S. Rim, C. H. Yi, and C. M. Kim, Opt. Express **21**, 32508 (2013).
[20] C. Dembowski, H. D. Gräf, A. Heine, R. Hofferbert, H. Rehfeld, and A. Richter, Phys. Rev. Lett. **84**, 867 (2000).
[21] D. A. Steck, W. H. Oskay, and M. G. Raizen, Science **293**, 274 (2001).
[22] C. Eltschka and P. Schlagheck, Phys. Rev. Lett. **94**, 014101 (2005).
[23] Q. Song, L. Ge, B. Redding, and H. Cao, Phys. Rev. Lett. **108**, 243902 (2012).
[24] X. F. Jiang *et al.*, Science **358**, 344 (2017).
[25] C. Liu, A. Di Falco, D. Molinari, Y. Khan, B. S. Ooi, T. F. Krauss, and A. Fratalocchi, Nat. Photon. **7**, 473 (2013).
[26] S. Bittner *et al.*, Science **361**, 1225 (2018).
[27] S. Sunada, S. Shinohara, T. Fukushima, and T. Harayama, Phys. Rev. Lett. **116**, 203903 (2016).
[28] T. Harayama, S. Sunada, and S. Shinohara, Photon. Res. **5**, B39 (2017).
[29] H. C. Chang, G. Kioseoglou, E. H. Lee, J. Haetty, M. H. Na, Y. Xuan, H. Luo, A. Petrou, and A. N. Cartwright, Phys. Rev. A **62**, 013816 (2000).
[30] A. W. Poon, F. Courvoisier, and R. K. Chang, Opt. Lett. **26**, 632 (2001).
[31] J. Wiersig, Phys. Rev. A **67**, 023807 (2003).
[32] T. Nobis, E. M. Kaidashev, A. Rahm, M. Lorenz, and M. Grundmann, Phys. Rev. Lett. **93**, 103903 (2004).
[33] Y. D. Yang and Y. Z. Huang, Phys. Rev. A **76**, 023822 (2007).
[34] Y. Z. Huang, K. J. Che, Y. D. Yang, S. J. Wang, Y. Du, and Z. C. Fan, Opt. Lett. **33**2170 (2008).
[35] Y. D. Yang and Y. Z. Huang, J. Phys. D: Appl. Phys. **49**, 253001 (2016).
[36] S. Bittner, C. Lafargue, I. Gozhyk, N. Djellali, L. Milliet, D. T. Hickox-Young, C. Ulysse, D. Bouche, R. Dubertrand, E. Bogomolny, J. Zyss, and M. Lebental, Europhys. Lett. **113**, 54002 (2016).
[37] S. Bittner, A. Loirette-Pelous, C. Lafargue, I. Gozhyk, C. Ulysse, B. Dietz, J. Zyss, and M. Lebental, Phys. Rev. A, **97**, 043826 (2018).
[38] H. Z. Weng, Y. Z. Huang, Y. D. Yang, X. W. Ma, J. L. Xiao, and Y. Du, Phys. Rev. A **95**, 013833 (2017).
[39] H. Z. Weng, Y. D. Yang, J. L. Xiao, Y. Z. Hao, and Y. Z. Huang, Opt. Express, **26**, 9409 (2018).
[40] S. Sridhar, Phys. Rev. Lett. **67**, 785 (1991).
[41] S.-B. Lee, J.-H. Lee, J.-S. Chang, H.-J. Moon, S. W. Kim, and K. An, Phys. Rev. Lett. **88**, 033903 (2002).
[42] E. J. Heller, Phys. Rev. Lett. **53**, 1515 (1984).
[43] P. So, E. Ott, S. J. Schiff, D. T. Kaplan, T. Sauer, and C. Grebogi, Phys. Rev. Lett. **76**, 4705 (1996).
[44] O. Biham and W. Wenzel, Phys. Rev. Lett. **63**, 819 (1989).
[45] J. Andreasen, H. Cao, J. Wiersig, and A. E. Motter, Phys. Rev. Lett. **103**, 154101 (2009).
[46] E. G. Altmann, T. Friedrich, A. E. Motter, H. Kantz, and A. Richter, Phys. Rev. E **77**, 016205 (2008).

[47] J. Wiersig, Phys. Rev. Lett. **97**, 253901 (2006).
[48] Y. D. Yang and Y. Z. Huang, IEEE J. Quantum Electron. **43**, 497 (2007).
[49] Q. Song, L. Ge, J. Wiersig, and H. Cao, Phys. Rev. A **88**, 023834 (2013).
[50] O. Svelto, *Principle of Lasers*, 5th ed. (Springer, Boston, MA, 2010).
[51] H. G. Schwefel, N. B. Rex, H. E. Tureci, R. K. Chang, A. D. Stone, T. Ben-Messaoud, and J. Zyss, J. Opt. Soc. Amer. B **21**, 923 (2004).
[52] B. Crespi, G. Perez, and S. J. Chang, Phys. Rev. E **47**, 986 (1993).
[53] M. Hentschel, H. Schomerus, and R. Schubert, Europhys Lett. **62**, 636 (2003).